Real-time Optimization and Adaptation of the Crosswind Flight of Tethered Wings for Airborne Wind Energy

Aldo U. Zgraggen*, Lorenzo Fagiano, *Member, IEEE,* and Manfred Morari, *Fellow, IEEE*

***Abstract*—Airborne wind energy systems aim to generate renewable energy by means of the aerodynamic lift produced by a wing tethered to the ground and controlled to fly crosswind paths. The problem of maximizing the average power developed by the generator, in presence of limited information on wind speed and direction, is considered. At constant tether speed operation, the power is related to the traction force generated by the wing. First, a study of the traction force is presented for a general path parametrization. In particular, the sensitivity of the traction force on the path parameters is analyzed. Then, the results of this analysis are exploited to design an algorithm to maximize the force, hence the power, in real-time. The algorithm uses only the measured traction force on the tether and the wing's position, and it is able to adapt the system's operation to maximize the average force with uncertain and time-varying wind. The influence of inaccurate sensor readings and turbulent wind are also discussed. The presented algorithm is not dependent on a specific hardware setup and can act as an extension of existing control structures. Both numerical simulations and experimental results are presented to highlight the effectiveness of the approach.**

I. Introduction

AIRBORNE wind energy (AWE) systems [1], [2] aim to harness wind energy beyond the altitude of traditional wind mills, in stronger and more steady winds, using tethered wings. The tethers are used to transfer the energy down to the ground. In particular, depending on the system layout, the traction force applied by the wing on the tethers is used to drive generators on the ground, or the energy from on-board generators is transferred via an electrified tether to the ground unit. To increase the power output, the wings are controlled to fly roughly perpendicular to the wind direction [3], in so-called crosswind paths. In the recent past, an increasing number of research groups in academia and industry started to develop new concepts of AWE systems, see e.g. [1], [4]–[15]. The automatic control of the tethered wings plays a major role for the efficiency and thus also economics of such energy generators. The goal is to control the wing in order to fly a crosswind path under constraints such as actuator or wing position limitations, while maximizing the generated power. In order to maximize the power output, the wing should fly on a path that yields the highest traction force for the given wind condition. This problem has been studied by several research groups, see [11]–[13], [16]–[21]. Most of these approaches employ an optimal path, computed off-line for specific wind conditions based on a nonlinear point-mass model. An automatic controller is then designed to follow this optimal reference trajectory. Yet, the offline generated optimal trajectories are subject to model-plant mismatch, hence they may be sub-optimal or even infeasible in practice. Moreover, when on-line optimization is used, like in Model Predictive Control approaches, the solution of a complex nonlinear optimization problem is required in real-time, which can be difficult and unreliable. Finally, the mentioned approaches assume that the wind speed and direction at the wing's location are known in order to employ the computed optimal path. However, the wind field changes over distance and time and it is difficult to estimate with only a few measurement points, like those available with ground anemometers.

In order to tackle these issues, in this paper we propose an optimization approach, for the real-time adaptation of the flown paths, assuming no exact knowledge of the wind condition. The approach does not employ a dynamical model of the wing for the optimization, hence avoiding potential problems due to model uncertainty. The algorithm works as an extension to an existing controller able to fly a tethered wing on periodic paths. At first, we analyze the influence of the crosswind path on the traction force, in order to asses the most important aspects of the flown trajectory for the sake of power generation. The results indicate that the location of the path with respect to the wind direction and vertical profile has much greater importance than its shape. Then, we introduce a real-time optimization algorithm aimed to improve and adapt the location, rather than the shape, of a given flown crosswind path using only the measurements of the wing's position relative to the ground unit and of the traction forces, i.e. no knowledge of the wind direction or profile. Additionally, we investigate the effects of erroneous sensor readings and turbulent wind on the performance of the adaptation, showing that the first do not affect the algorithm but the latter can slow down the convergence. We present the results obtained by applying the approach in numerical simulations as well as in real-world experiments.

A. Zgraggen and M. Morari are with the Automatic Control Laboratory, ETH Zürich, Switzerland. E-mail: zgraggen|morari@control.ee.ethz.ch

L. Fagiano is with ABB Switzerland Ltd., Corporate Research, Baden-Dättwil, Switzerland. E-mail: lorenzo.fagiano@ch.abb.com

This research has received funding from the California Energy Commission under the EISG grant n. 56983A/10-15 "Autonomous flexible wings for high-altitude wind energy generation", from the European Union Seventh Framework Programme (FP7/2007-2013) under grant agreement n. PIOF-GA-2009-252284 - Marie Curie project "Innovative Control, Identification and Estimation Methodologies for Sustainable Energy Technologies", and from the Swiss Competence Center Energy and Mobility (CCEM).

* Corresponding author: zgraggen@control.ee.ethz.ch.

The paper is organized as follows. We explain the system under consideration and elaborate the problem formulation in Section II. Then, we present a study of the traction force of a tethered wing for a flown path in Section III. Based on this analysis, the proposed algorithm to maximize the traction force is described in Section IV. In Section V the influence of sensor noise and wind turbulences on the algorithm are discussed. In Section VI numerical simulations and results from test flights with a small scale prototype are presented.

II. System Description and Problem Formulation

We consider an AWE generator that exploits aerodynamic lift to produce electrical energy. For an overview of such systems, see e.g. [1], [2]. The main components of the generator are the ground unit, the tether, and the wing. The tether is used to anchor the wing to the ground unit, where realizations with one or multiple tethers are possible. The wing is flown on a periodic path, sustained by the aerodynamic lift, which results in a traction force F on the tether. The electricity is either generated on-board of the wing, with small propellers and on-board generators [4], or in the ground unit, by unreeling the tether from drums connected to generators [6]–[8].

We define a right-handed inertial coordinate system $(\mathbf{e}_x, \mathbf{e}_y, \mathbf{e}_z)$, fixed to the ground unit (see Fig. 1). The unit vectors $\mathbf{e}_x$ and $\mathbf{e}_y$ are parallel to the ground and $\mathbf{e}_z$ is vertical with respect to the ground and pointing upwards. The wing's position p is described by spherical coordinates consisting of the two angles φ and ϑ and the tether length r. Assuming a straight tether, the azimuthal angle φ defines the angle between the projection of the tether on the ground and the $\mathbf{e}_x$ axis, while the elevation ϑ represents the angle between the tether and the ground plane $(\mathbf{e}_x, \mathbf{e}_y)$. We assume that the incoming wind is parallel to the ground, i.e. the $(\mathbf{e}_x, \mathbf{e}_y)$-plane, and its misalignment with respect to $\mathbf{e}_x$ is denoted by φ_W, see Fig. 1.

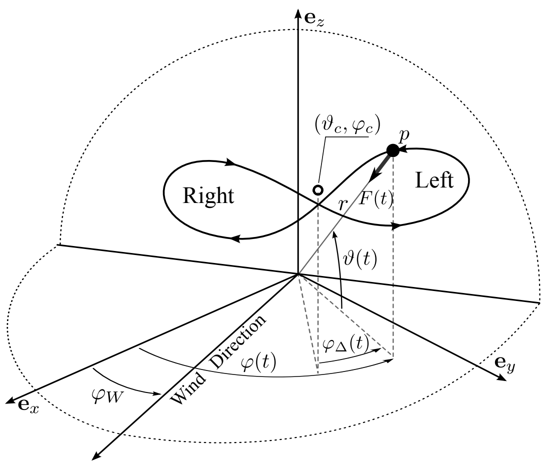

Fig. 1. The wing's position p (black dot) is shown on a figure eight path. Note the arrows on the path, indicating an "up-loop" flight pattern (i.e. the wing climbs up on the side of the path and dives in the middle). The wind window is depicted with dotted lines. The average location of the path (circle) is denoted by (φ_c, ϑ_c). The prevalent wind direction forms an angle φ_W with the fixed axis $\mathbf{e}_x$.

Due to boundary layer flow effects of the wind above the earth's surface, the magnitude of the wind W is a function of the altitude z above the ground, the so-called wind shear effect. Common choices to model such a wind shear are the log or the power laws [22]. In this paper, we consider the latter, but the results hold for a general monotonically increasing wind profile. In our coordinate system, the altitude is given by $z = r \sin\vartheta$ and the power law is defined as

$$W(\vartheta) = W_0 \left(\frac{r \sin\vartheta}{Z_0} \right)^{\alpha}, \tag{1}$$

where W_0 is the reference wind speed at the reference altitude Z_0 and α is the power law exponent, which depends on the roughness of the surface [22]. In Fig. 2 an example of such a wind profile is given.

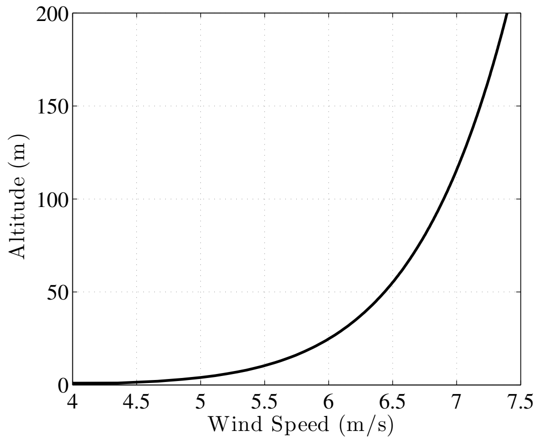

Fig. 2. Wind profile defined by the power law with $W_0 = 5\,\text{m/s}$, $Z_0 = 4\,\text{m}$, and $\alpha = 0.1$

In AWE systems, during power generation the tethered wing cannot fly upwind, surpassing its anchor point against the wind. Thus, its motion is restricted on a quarter sphere defined by the tether length r, the ground plane $(\mathbf{e}_x, \mathbf{e}_y)$, and a vertical plane perpendicular to the prevalent direction of the wind field and containing the anchor point of the tether (see Fig. 1, dotted lines). This quarter sphere is called "wind window". The wing is assumed to fly periodic paths in the wind window, under the action of a feedback controller K. Such a path can be described by a set of points in the (φ, ϑ)-plane. The average position of the path is denoted by (φ_c, ϑ_c). The angular distances from such an average position to each point on the path in φ and ϑ directions are denoted by φ_Δ and ϑ_Δ, respectively. By introducing the continuous time variable t, we can define the corresponding trajectory as the pair

$$\varphi(t) = \varphi_c + \varphi_\Delta(t), \qquad \vartheta(t) = \vartheta_c + \vartheta_\Delta(t)$$

with the trajectory period T to complete one closed path, i.e.

$$\varphi_\Delta(t+T) = \varphi_\Delta(t), \qquad \vartheta_\Delta(t+T) = \vartheta_\Delta(t).$$

We define the left and right half paths as the points where $\varphi_\Delta(t) \geq 0$ and $\varphi_\Delta(t) < 0$, respectively.

For systems with multiple tethers, the path has to be such that the tethers do not coil up during one full period and therefore we will consider paths shaped like an eight, see e.g. [12], flying up-loops. This means the wing flies upwards on the side and down in the center of the figure eight, see Fig. 1. For the remainder of this paper we will call one closed path a "loop" or "path" to refer to a single flown figure eight. We assume that the path is symmetric w.r.t. a line in the (φ, ϑ)-plane. The angle between this symmetry line and the line $\varphi = \varphi_c$ is denoted with β, named the "inclination" of the path. The range of φ_Δ values is $[-\varphi_\Delta^{max}, \varphi_\Delta^{max}]$ with $\varphi_\Delta^{max} > 0$. The maximal $\varphi_\Delta(t)$ value, φ_Δ^{max}, defines the lateral span of the path, since it accounts for half of the total lateral span. Similarly, the range of ϑ_Δ values is $[-\vartheta_\Delta^{max}, \vartheta_\Delta^{max}]$ with $\vartheta_\Delta^{max} > 0$. The maximal $\vartheta_\Delta(t)$ value, ϑ_Δ^{max}, defines the vertical span of the path. See Fig. 1 and 3 for a graphical representation.

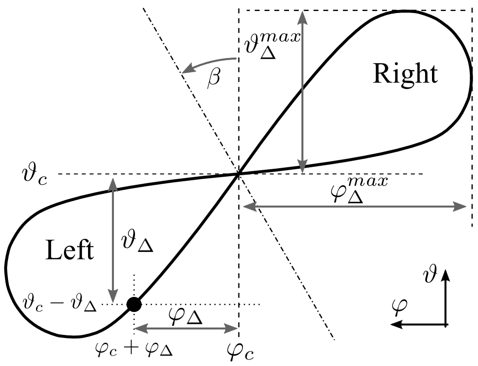

Fig. 3. A generic inclined path with average position (φ_c, ϑ_c) plotted in the $(\varphi$-$\vartheta)$-plane. The φ and ϑ coordinates are depicted as seen from the ground unit and looking at the wing, note the orientation of the φ axis. A generic point on the left half path is shown as a black dot. The angle β defines the inclination of the path, whose symmetry line is shown as dash-dotted line.

The dynamics of the system can generally be described as

$$\begin{aligned} \dot{x} &= f(x, u, \varphi_W, W_0, Z_0, \alpha) \\ y &= g(x, u)\,, \end{aligned} \tag{2}$$

where x denotes the states, u the control input, and y the measured output. The wind cannot be easily measured or estimated, hence we assume that the wind direction φ_W and parameters W_0, Z_0, α are not precisely known. The control input u is computed by the controller K, which is a discrete-time system with internal state z, input y, and parameters Θ.

$$K : \begin{cases} z(\tau+1) &= h_z(z(\tau), y(\tau), \Theta(\tau)) \\ u(t) &= h_u(z(\tau), y(\tau), \Theta(\tau)), \quad \forall t \in [\tau T_s, (\tau+1)T_s) \end{cases},$$

where $\tau \in \mathbb{N}$ is the discrete sampling instant and T_s the sampling time. The parameters Θ contain specifications of the path to be flown by the wing, namely the average position of the path (φ_c, ϑ_c), its spans φ_Δ^{max} and ϑ_Δ^{max}, and inclination β:

$$\Theta \doteq (\varphi_c, \vartheta_c, \varphi_\Delta^{max}, \vartheta_\Delta^{max}, \beta)\,, \tag{3}$$

It is assumed that the controller K is able to attain such specifications, see e.g. [23].

The average power $\bar{P}$ produced by an AWE generator with generators on the ground during one full path with period T is

$$\bar{P} = \frac{1}{T}\int_0^T \dot{r}(t)\, F(t) dt\,,$$

where $\dot{r}$ is the reel-out speed of the tether and $F(t)$ is the traction force at time t. As it is done in several previous work, see e.g. [3], [13], we consider power production at a constant reel-out speed. Hence, we obtain:

$$\bar{P} = \dot{r}\,\bar{F}\,,$$

where

$$\bar{F} = \frac{1}{T}\int_0^T F(t) dt\,. \tag{4}$$

Thus, in this framework the maximization of the average traction force implies maximization of the average power produced during the path. This also holds for systems with on-board generation where turbines are installed on the wing, since the obtained apparent wind speed is directly related to the traction force [3].

In the considered settings, $\bar{F}$ is a function of the controller's parameters Θ, i.e. our decision variables, and of the wind field, described here by its direction φ_W and wind shear parameters W_0, Z_0, α, which are uncertain. Our aim is to find the parameters Θ such that the average traction force (hence the average power) is maximal. The related optimization problem can be formulated as

$$\max_{\Theta} \qquad \bar{F}(\Theta, \varphi_W, W_0, Z_0, \alpha)\,. \tag{5}$$

The exact solution of (5) would require the precise knowledge of the wind profile and direction, which are not assumed to be available here. Light detection and ranging (LIDAR) systems could be used to gather information on the wind profile and direction. However, apart from their relatively high cost, these systems provide a measurement of the wind along a single direction, so that three beams should be coordinated to obtain a measure of the wind vector at a single point in space. Such information would be valuable to have an approximate idea of the wind field, but it would be still too scarce to optimize the flown path. Therefore, we will propose a strategy where the wind at the wing's location does not need to be measured. If available, a LIDAR could then be used to obtain a first estimate of the wind direction and speed to initialize our method. In order to tackle this problem, we proceed in two steps. At first, we analyze the influence of Θ on the average traction force; then, on the basis of such analysis we derive a real-time optimization/adaptation algorithm, to be used on top of controller K, able to solve (5) by dealing with the uncertainty of the wind direction and profile, exploiting the measure of the traction force acting on the tethers. For simplicity, in the following we assume the tether length r to be constant, which is a special case of a constant reel-out speed.

III. Sensitivity Analysis of the Crosswind Traction Force

In this section, we will first investigate the properties of the average traction force for a flown path using a simplified model. The advantage of such a model is that it allows one to carry out an analytical study of the traction force as a function of the parameters Θ. The results of this first analysis are then compared to simulations of a dynamical non-linear point-mass model of the system. The latter is derived from first principle equations and includes effects from gravity and inertial forces.

A. Analysis of the traction force with a simplified model

A simplified model to estimate the traction force of a tethered wing depending on its location has been introduced in [3] and subsequently refined in several contributions, for a detailed derivation see e.g. [3], [24]. According to this model, for a constant reeling speed and fixed values of W_0, Z_0, α, the traction force F is a function of the current location of the wing and of the wind direction:

$$F(\vartheta, \varphi, \varphi_W) = \mathcal{C}\, v(\vartheta)\, m(\varphi - \varphi_W), \tag{6}$$

where

$$\mathcal{C} = \frac{1}{2}\rho A C_L E_{eq}^2 \left(1 + \frac{1}{E_{eq}^2}\right)^{\frac{3}{2}} \tag{7}$$
$$v(\vartheta) = W(\vartheta)^2 \cos(\vartheta)^2$$
$$m(\varphi - \varphi_W) = \cos(\varphi - \varphi_W)^2$$

and

$$E_{eq} = \frac{C_L}{C_{D,eq}} = \frac{C_L}{C_D + \frac{C_{D,l} A_l}{4A}}. \tag{8}$$

In (7)-(8), the air density is indicated by ρ, A is the wing reference area, C_L is the wing's lift coefficient, $C_{D,eq}$ is the equivalent drag coefficient, accounting for the drag of the wing and the added drag by the cable. $C_{D,l}$ is the drag coefficient of the cable and $A_l = n_l\, r\, d_l$ is the cable reference area, where n_l is the number of lines holding the wing, r is the line length, and d_l is the line diameter. The values of C_L and C_D generally depend on the angle of attack and its derivative, which influence the aerodynamics of the wing. However, these coefficients typically do not change much during energy generation. Hence, we assume them to be constant for simplicity, as considered e.g. in [11]. For a given wind field, the simplified model (6) provides us with a theoretical value of the traction force as a function of the wing's location. Such a theoretical value is obtained by neglecting all forces except for the aerodynamic ones and the cable tension.

By inspection, function $m(\varphi - \varphi_W) : (\varphi_W - \pi/2, \varphi_W + \pi/2) \mapsto (0, 1]$ in (6)-(8) is quasi-concave with its maximum at $\varphi = \varphi_W$. Function $v(\vartheta) : (0, \pi/2) \mapsto \mathbb{R}^+$ consists of two parts. The first part, the wind profile $W(\vartheta)$, is assumed to be monotonically increasing, according to the wind shear model in (1), and the second part, $\cos(\vartheta)^2$, is also a quasi-concave function in the domain of v. By using the second-order condition for quasi-concave functions [25], it can be verified that the product (see Fig. 4 for a typical example) is still quasi-concave and that the point (φ, ϑ) providing maximal traction force for (6) is given by $(\varphi, \vartheta) = (\varphi_W, \arctan(\sqrt{\alpha}))$.

Equations (6)-(8) allow us to carry out an analysis of the traction force as a function of the parameters Θ. By introducing the index $k = 1, \ldots, N$, which identifies the samples of a discretized path with sampling time T_s, any sampled position

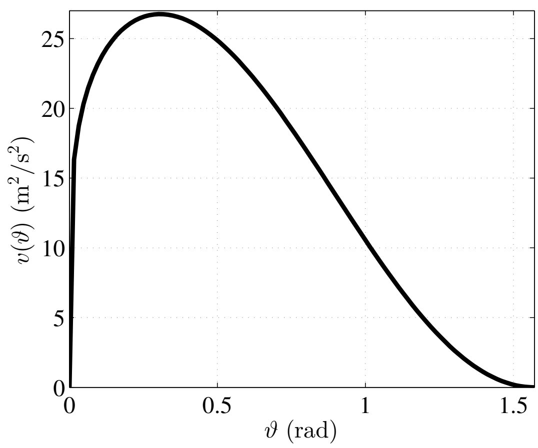

Fig. 4. Quasi-concave function $v(\vartheta)$ with $r = 30\,\mathrm{m}$, $W_0 = 5\,\mathrm{m/s}$, $Z_0 = 4\,\mathrm{m}$, and $\alpha = 0.1$.

in the path can be expressed as $(\varphi_c + \varphi_\Delta(k), \vartheta_c + \vartheta_\Delta(k))$. The discrete form of the average traction force (4) can then be written as

$$\frac{1}{T}\int_0^T F(t)dt \simeq \frac{1}{NT_s}\sum_{k=1}^{N} F(k) T_s = \frac{1}{N}\sum_{k=1}^{N} F(k).$$

The average traction force $\bar{F}$ for one period of the path is thus given by

$$\bar{F}(\Theta, \varphi_W,) = \frac{1}{N}\sum_{k=1}^{N} \mathcal{C}\, v(\vartheta(k))\, m(\varphi(k) - \varphi_W), \tag{9}$$
$$\text{with} \quad \begin{array}{l} \vartheta(k) = \vartheta_c + \vartheta_\Delta(k) \\ \varphi(k) = \varphi_c + \varphi_\Delta(k) \end{array}.$$

For the following analysis, we focus on the dependence of $\bar{F}$ on φ_c, ϑ_c, φ_Δ^{max}, and ϑ_Δ^{max} only, and fix the inclination $\beta = 0$ (see Fig. 3). Since the wing is assumed to fly within the wind window, we limit the analysis to the following ranges:

$$\begin{aligned} \varphi_c &\in (\varphi_W - \pi/2, \varphi_W + \pi/2) \\ \vartheta_c &\in (0, \pi/2) \\ \varphi_\Delta^{max} &\in (0, \pi/2 - (\varphi_c - \varphi_W)] \\ \vartheta_\Delta^{max} &\in (0, \min(\vartheta_c, \pi/2 - \vartheta_c)] \end{aligned}$$

In Fig. 5, the average traction force (9) as a function of $\varphi_c - \varphi_W$ for three different values of ϑ_c is shown. Note that the forces in all the plots have been normalized with the maximum force value of the sample in order to emphasize the independence of the qualitative behavior on the wind: stronger winds influence only the numerical values, but the shape of the curve remains unchanged. By changing the elevation of the path, ϑ_c, the value of $\bar{F}$ changes according to the value of $v(\vartheta)$ from (7) (see Fig. 5). In particular, as it can be inferred by the above-reported discussion on the concavity of the force as a function of ϑ, there is a single value of ϑ_c that maximizes the traction force, and this value depends only on the wind profile and not on the misalignment $(\varphi_W - \varphi_c)$.

From (9), we can notice that the contribution of the left and right half-paths to the average traction force $\bar{F}$ are not the same if $\varphi_c \neq \varphi_W$. We therefore derive the average traction forces for each of the half-paths, and investigate the influence

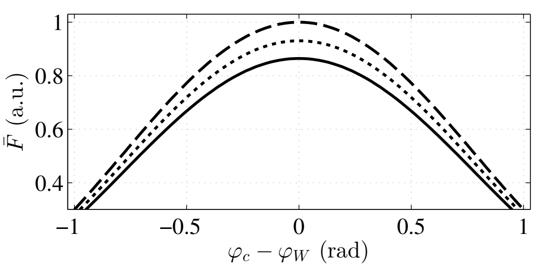

Fig. 5. Average traction force computed with the simplified model with the spans of the path $\varphi_\Delta^{max} = 0.15\,\text{rad}$ and $\vartheta_\Delta^{max} = 0.05\,\text{rad}$. Solid: $\vartheta_c = 0.1\,\text{rad}$, dashed: $\vartheta_c = 0.3\,\text{rad}$, and dotted: $\vartheta_c = 0.5\,\text{rad}$.

of the parameters Θ on their difference. The average traction forces of the left and right half paths are:

$$\begin{aligned}\bar{F}_L &= \frac{1}{N_L}\sum_{k=1}^{N}\{\mathcal{C}v(\vartheta(k))m(\varphi(k)-\varphi_W)|\varphi(k)\geq\varphi_c\}\\ \bar{F}_R &= \frac{1}{N_R}\sum_{k=1}^{N}\{\mathcal{C}v(\vartheta(k))m(\varphi(k)-\varphi_W)|\varphi(k)<\varphi_c\}\,,\end{aligned} \tag{10}$$

where $\bar{F}_L$ stands for the average traction force of the left half and $\bar{F}_R$ for the right half. N_L and N_R are the number of samples on the left and right half paths, respectively, i.e. $N = N_L + N_R$.

The traction force difference between the left and right half-paths, using (7) and (10), is given, after some manipulations and assuming a sufficiently small sampling time, by

$$\Delta\bar{F}(\Theta,\varphi_W) = \bar{F}_L - \bar{F}_R \simeq -\frac{\mathcal{C}}{2}\sin(2(\varphi_c-\varphi_W))\mathcal{B}, \tag{11}$$

where the positive term $\mathcal{B}$ is given by

$$\begin{aligned}\mathcal{B} = &\frac{1}{N_L}\sum_{k=1}^{N}\{v(\vartheta(k))\sin(2|\varphi_\Delta(k)|)\,|\varphi(k)\geq\varphi_c\}\\ &+\frac{1}{N_R}\sum_{k=1}^{N}\{v(\vartheta(k))\sin(2|\varphi_\Delta(k)|)\,|\varphi(k)<\varphi_c\}\,.\end{aligned}$$

From (11) it can be seen that the difference in traction force is zero only if $\varphi_c = \varphi_W$, i.e. the path is centered w.r.t. the wind, and that it is monotonic for $|\varphi_c - \varphi_W| \leq \pi/4$. Moreover, paths with an average position on the left of the wind direction, as seen from the anchor point of the tether (i.e. $\varphi_c - \varphi_W > 0$), have a negative $\Delta\bar{F}$, and vice-versa, see Fig. 6 where the left-right difference in average traction force (11) as a function of $\varphi_c - \varphi_W$ for different values of ϑ_c is shown. This comes from the fact that the half-path farther away from the wind direction experiences a smaller fraction of the incoming wind in tether direction, thus generating less traction force. In Fig. 7, a plot of $\Delta\bar{F}$ for different values of the half-span φ_Δ^{max} is shown. By changing the span of the path, the magnitude of $\Delta\bar{F}$ changes. For larger spans, the difference between the average traction force given by the left and right half-paths gets larger, since the average wind conditions for the two halves differ more. The lateral span of the path has also an influence on the average traction force, see Fig. 8, i.e. wider paths provide smaller average traction force. Thus, a path which has a higher traction force due to its small span will also have a smaller magnitude in $\Delta\bar{F}$ (compare Figs. 7 and 8). Note that the value of ϑ_c has an effect on the average traction force difference, too, but this is not as large as that of the span of the path in φ direction (compare Figs. 6 and 7).

The span ϑ_Δ^{max} also has an influence on the average traction force $\bar{F}$ and on the difference of left-right average traction forces $\Delta\bar{F}$ as shown in Fig. 9 and Fig. 10, respectively. Comparing Figs. 7-10, it can be seen that the span φ_Δ^{max} has more influence on the difference between left and right average traction forces whereas ϑ_Δ^{max} has more influence on the total average traction force.

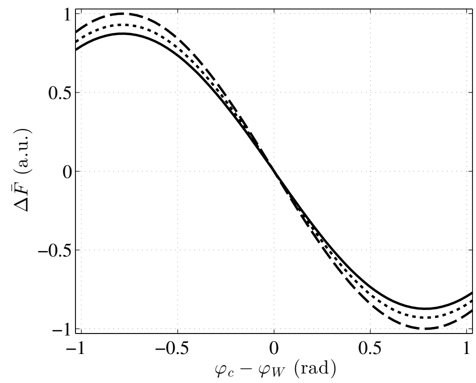

Fig. 6. Difference of average traction force $\Delta\bar{F}$ computed with the simplified model, with spans of the path $\varphi_\Delta^{max} = 0.3\,\text{rad}$ and $\vartheta_\Delta^{max} = 0.05\,\text{rad}$. Solid: $\vartheta_c = 0.1\,\text{rad}$, dashed: $\vartheta_c = 0.3\,\text{rad}$, and dotted: $\vartheta_c = 0.5\,\text{rad}$.

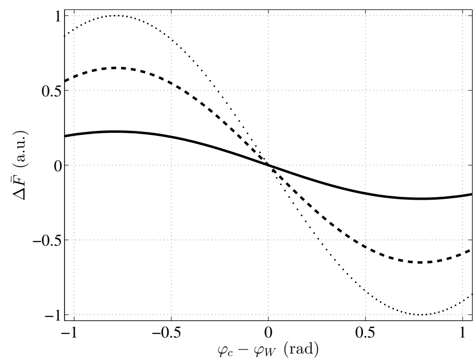

Fig. 7. Difference of average traction forces $\Delta\bar{F}$ computed with the simplified model, with $\vartheta_c = 0.2$, $\vartheta_\Delta^{max} = 0.1\,\text{rad}$, and different values of the lateral span. Solid: $\varphi_\Delta^{max} = 0.1$, dashed: $\varphi_\Delta^{max} = 0.3$, and dotted: $\varphi_\Delta^{max} = 0.5$.

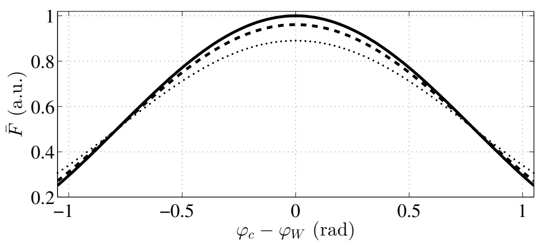

Fig. 8. Average traction force $\bar{F}$ computed with the simplified model, with $\vartheta_c = 0.2$, $\vartheta_\Delta^{max} = 0.1\,\text{rad}$, and different values of the lateral span φ_Δ^{max}. Solid: $\varphi_\Delta^{max} = 0.1$, dashed: $\varphi_\Delta^{max} = 0.3$,and dotted: $\varphi_\Delta^{max} = 0.5$.

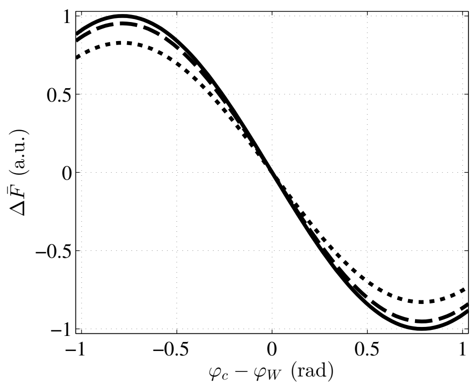

Fig. 9. Difference of average traction force $\Delta\bar{F}$ computed with the simplified model, with $\vartheta_c = 0.5$ and a lateral span of the path $\varphi_\Delta^{max} = 0.15$ rad. Solid: $\vartheta_\Delta^{max} = 0.05$ rad, dashed: $\vartheta_\Delta^{max} = 0.25$ rad, and dotted: $\vartheta_\Delta^{max} = 0.45$ rad.

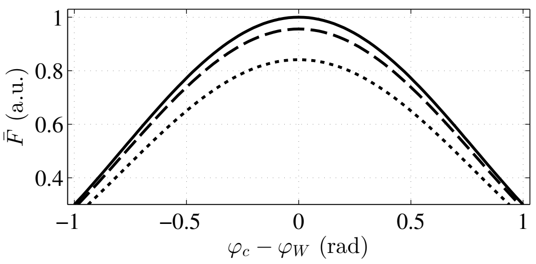

Fig. 10. Average traction force $\bar{F}$ computed with the simplified model, with $\vartheta_c = 0.5$ and a lateral span of the path $\varphi_\Delta^{max} = 0.15$ rad. Solid: $\vartheta_\Delta^{max} = 0.05$ rad, dashed: $\vartheta_\Delta^{max} = 0.25$ rad, and dotted: $\vartheta_\Delta^{max} = 0.45$ rad.

B. Analysis of the traction force with a dynamic model

In this section, we employ a dynamic model to asses, via numerical simulations, the considerations derived with the simplified model, and to analyze also the effects of different path inclinations β. The dynamics $f(x, u, \varphi_W, W_0, Z_0, \alpha)$ are modeled here by the widely used nonlinear point-mass model for a tethered wing, see e.g. [11]–[13], [17], [20], [21]. The dynamic equations are derived from first principles and the wing is assumed to be a point with given mass. The tether is assumed to be straight with a non-zero diameter. The aerodynamic drag of the tether and half of the tether mass are added to the wing's drag and mass, respectively. The aerodynamic forces are modeled with constant lift and drag coefficients, and effects from gravity and inertial forces are included. The wing is assumed to be steered by a change of the roll angle ψ, which is manipulated by a control system, and thus, referring to (2), we have $u = \psi$. The state x of this system is given by $x = (\varphi, \vartheta, r, \dot{\varphi}, \dot{\vartheta}, \dot{r})$.

In order to carry out the simulations, the controller K is designed using the approach described in [23]. Such a controller is able to make the wing fly on a symmetric figure eight path with the required spans and inclination, and with the average position being a given reference location (φ_c, ϑ_c).

Consistently with Section III-A, the average traction forces generated during the full path and the average traction force generated on the left and right half paths are computed from the simulation results:

$$\bar{F}(\Theta, \varphi_W) = \frac{1}{N}\sum_{k=1}^{N} F(k) \tag{12}$$

$$\begin{aligned} \bar{F}_L &= \frac{1}{N_L}\sum_{k=1}^{N} \{F(k) \,|\, \varphi(k) \geq \varphi_c\} \\ \bar{F}_R &= \frac{1}{N_R}\sum_{k=1}^{N} \{F(k) \,|\, \varphi(k) < \varphi_c\} \end{aligned} \tag{13}$$

The traction force difference between the left and right half path is

$$\Delta\bar{F}(\Theta, \varphi_W) = \bar{F}_L - \bar{F}_R\,. \tag{14}$$

As done before, we want to study how the average traction force and the difference in average traction force between the left and right half paths change for different values of Θ, including this time also the inclination β, in the range $\beta \in [-\pi/2, \pi/2]$.

Comparing the traction force for various φ_c and ϑ_c with a symmetric horizontal path shape (i.e. $\beta = 0$) shows good qualitative correspondence with the simplified model used in Section III-A. See Fig. 11 for a comparison of the two models. The numerical values differ slightly between the two models due to the assumptions made in the simplified model but more importantly the qualitative shape stays the same, thus indicating that gravity and inertial forces do not have a large impact on the average forces. If the path is inclined, i.e. $\beta \neq 0$, the average traction force does not increase more than 2 % for φ_c around the optimum of $\bar{F}$, see Fig. 12, but the values of $\Delta\bar{F}$ change significantly. In fact, when the path is inclined, the traction force difference is not anymore zero for $\varphi_c - \varphi_W = 0$. A positive value of β corresponds to a negative value of $\varphi_c - \varphi_W$ such that $\Delta\bar{F} = 0$ and vice versa, see Fig. 13. The effect of larger spans in the presence of $\beta \neq 0$ is the same as the one observed in Section III-A, e.g. a larger value of φ_Δ^{max} increases $\Delta\bar{F}$ for fixed values of the other parameters. As expected from the analysis with the simplified model, stronger wind or different tether length r do not affect the qualitative results.

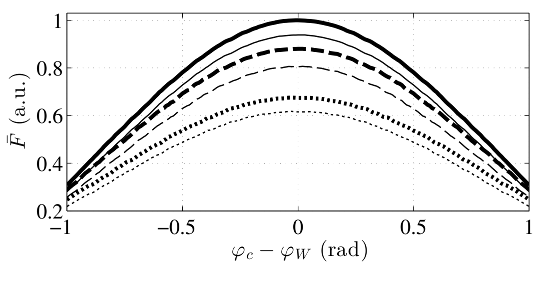

Fig. 11. Average traction force $\bar{F}$, as a function of $\varphi_c - \varphi_W$, computed with the simplified model (thin lines) and with the point-mass model (thick lines) for three different values of ϑ_c: $\vartheta_c = 0.3$ (solid), $\vartheta_c = 0.5$ (dashed), and $\vartheta_c = 0.7$ (dotted).

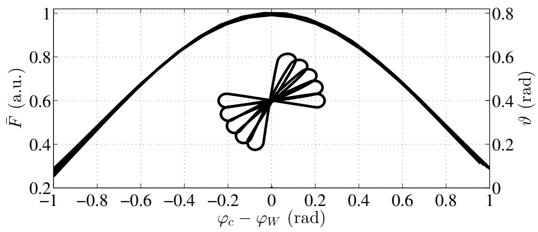

Fig. 12. Traction force $\bar{F}$ computed with the point-mass model, as a function of $\varphi_c - \varphi_W$, with $\vartheta_c = 0.4$. There are five lines with values of $\beta = \{0, 0.3, 0.6, 0.9, 1.2\}$ rad. The resulting shapes of the path are depicted underneath the traction force curve; the corresponding y-axis, giving the values of ϑ for the flown path, is depicted on the right of the plot.

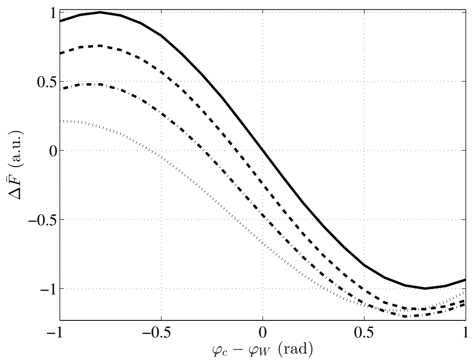

Fig. 13. Traction force difference $\Delta\bar{F}$ computed with the point-mass model for $\vartheta_c = 0.4$, $\varphi_\Delta^{max} = 0.24$, and different inclinations $\beta = 0$ (solid), $\beta = 0.3$ (dashed), $\beta = 0.6$ (dot-dashed), and $\beta = 0.9$ (dotted).

C. Discussion

The results of the previous two sections show that there is a single optimal average location, denoted as $(\varphi_c^*, \vartheta_c^*)$, yielding the maximal average traction force for a given path shape. In particular, we have $\varphi_c^* = \varphi_W$, while ϑ_c^* depends on the vertical wind profile. The average traction force is very sensitive on the average position of the path. A misalignment of φ_c with respect to φ_c^* of roughly 20° can lead to a decrease of average traction force of 15%, while 50% decrease of the force is obtained for a misalignment of roughly 45°, see Fig. 5. An average elevation $\vartheta_c \neq \vartheta_c^*$ can also reduce the traction force by a significant amount, in the same order as for φ_c. As an example, with an error in both φ_c and ϑ_c of around 20° from the optimum, the traction force will be reduced by almost 30%.

For horizontal paths (i.e. $\beta = 0$), the difference in average traction force, $\Delta\bar{F}$, is zero for an average position $\varphi_c = \varphi_W$ and it is monotonically increasing for values of $\varphi_c - \varphi_W$ between $\pi/4$ and $-\pi/4$. Moreover, the sign of $\Delta\bar{F}$ is the opposite w.r.t. that of $\varphi_c - \varphi_W$, i.e. $\varphi_c - \varphi_c^*$. Therefore, if $\beta = 0$ the value of $\Delta\bar{F}$ is a good indicator of the alignment of φ_c with the wind direction φ_W. As seen in Fig. 12, the inclination has only a small influence on the traction force, changing it less than 2% in the interval around the optimum. However, the average traction force difference between the left and right half paths is sensitive to changes in β. A positive value of β can decrease the magnitude of $\Delta\bar{F}$ on the right side of the wind window up to 75%, while increasing it on the left side by only around 20%. Thus, with $\beta \neq 0$ the difference in traction force $\Delta\bar{F}$ is not anymore zero for $\varphi_c = \varphi_W$, and its sign is not the opposite w.r.t the sign of the misalignment $\varphi_c - \varphi_W$ anymore (see Fig. 13).

As seen in Fig. 8, increasing the lateral span φ_Δ^{max} of the path by a factor of 5 decreases the average traction force roughly by 10%. A larger lateral span of the path scales up $\Delta\bar{F}$, but also decreases the average traction force $\bar{F}$. This could lead to the conclusion that the shorter the lateral span, the better it is in terms of system operation. This is only partially true. First, a short span implies sharp turns that induce more drag, slowing the wing down, hence decreasing the average traction force. However, this effect is not captured by the point-mass model considered here, thus leading to the result that paths with very small span do not lose performance in terms of traction force. Second, for a short span it might be difficult to infer something about the wind direction, due to the small value of $\Delta\bar{F}$. As seen in Fig. 10, increasing the vertical span ϑ_Δ^{max} of the path by a factor of 5 decreases the average traction force roughly by 15% and also decreases the magnitude of $\Delta\bar{F}$. This shows that a small vertical span ϑ_Δ^{max} of the path is favorable. This has two advantages. First, the wing does not need to overcome gravity to climb for a long distance and secondly it will stay closer to the targeted ϑ_c position.

In conclusion, the analysis above shows that optimizing the average position (φ_c, ϑ_c) yields the largest increase of average traction force (hence generated power). The shape of the path, in terms of lateral span and inclination, has only a relatively small influence on the traction force. Moreover, even an optimal path, in terms of shape, has to be flown at the optimal location in order not to lose a large fraction of the traction force. In the next section, we exploit these considerations to derive an algorithm able to optimize in real-time the average path location and to adapt it in the presence of changing wind direction φ_W, using only the measurements of the traction force on the tethers.

IV. Real-time Optimization and Adaptation Algorithm

As seen in the previous section, the average location of a flown path has the largest influence on the generated traction force among all of the considered parameters. Thus we aim to find the best average location in φ and ϑ for a given path shape, in order to maximize the average power output of the AWE system. Since the inclination of a path has an adverse effect on $\Delta\bar{F}$ and does not affect $\bar{F}$ much, we only consider horizontal paths with $\beta = 0$. Moreover, an inclined path can increase the difference between the maximal and minimal instantaneous traction force $F(t)$ between the left and right half-loops, leading to an asymmetric wear of the system's components. Enforcing a horizontal path can be done in practice with a suitable controller as in [23]. Motivated by these results, in the following we take only (φ_c, ϑ_c) as free optimization variables out of the considered parameters Θ in (3), while we fix the half-span φ_Δ^{max} and the vertical span ϑ_Δ^{max} to prescribed values and select $\beta = 0$.

Recall that we assume that the underlying controller K accepts reference values for the average location where the path should be flown. The algorithm we present next will then compute such reference values in order to solve the following optimization problem:

$$\max_{\vartheta_c,\varphi_c} \quad \bar{F}(\varphi_c,\vartheta_c,\varphi_W,W_0,Z_0,\alpha)\,. \tag{15}$$

In Fig. 14, a block diagram of such a system can be seen.

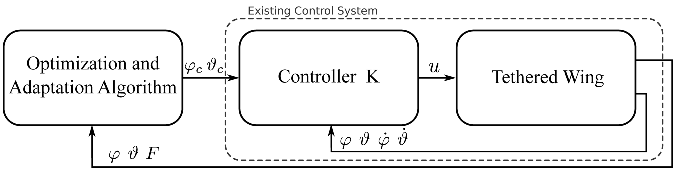

Fig. 14. A block diagram depicting the control system together with the optimization and adaptation algorithm.

We assume that the parameters $\varphi_W, W_0, Z_0, \alpha$, specifying the wind direction and profile, are not known, hence the optimization problem (15) is uncertain due to the lack of information on φ_W and the wind shear profile. On the other hand, we assume that the traction force F is measured, as well as the position of the wing w.r.t. the ground unit. Hence the values of $\bar{F}$ and $\Delta\bar{F}$ for each flown path are measured.

The analysis presented in the previous section indicates that we can reformulate the optimization problem (15) as

$$\max_{\vartheta_c}\left[\max_{\varphi_c} \quad \bar{F}(\varphi_c,\vartheta_c,\varphi_W,W_0,Z_0,\alpha)\right], \tag{16}$$

i.e. (16) can be maximized separately in φ_c and ϑ_c, since the value of φ_c that maximizes the average traction force, for given ϑ_c, depends only on φ_W and not on ϑ_c itself and, vice-versa, the optimal value ϑ_c^* does not depend on φ_c. Also, note that for horizontal paths we have, irrespective of ϑ_c,

$$\arg\max_{\varphi_c} \bar{F}(\varphi_c,\vartheta_c,\varphi_W,W_0,Z_0,\alpha) = \arg\min_{\varphi_c} |\Delta\bar{F}(\varphi_c,\vartheta_c,\varphi_W,W_0,Z_0,\alpha)|$$

as it can be derived from (9) and (11) and from the results in Section III-B. Therefore, the problem (15) can be solved by addressing two subsequent optimization problems independently. We will first exploit the measure of $\Delta\bar{F}$ to find the best location in φ, i.e. to compute $\arg\min_{\varphi_c} |\Delta\bar{F}(\varphi_c,\vartheta_c,\varphi_W,W_0,Z_0,\alpha)|$, and then the measure of $\bar{F}$ to find the best location in ϑ, i.e. solving (16) with the previously found optimal φ_c. The advantage of using the differences in average traction forces to find the optimal φ_c, instead of using only $\bar{F}$, is that a single value of $\Delta\bar{F}$, i.e. a single flown path, gives already an indication on the sign of the misalignment $\varphi_c - \varphi_W$, hence on the search direction for φ_c. By using only $\bar{F}$, the values obtained by two paths with different φ_c would be needed to estimate the search direction, which would take at least twice as long. Thus, the adaptation in φ direction is sped up by looking at the traction force difference $\Delta\bar{F}$ instead of the total average traction force $\bar{F}$ only.

A. Algorithm Outline

We present a short outline of an algorithm able to adapt the average position of a path, such that it converges to the optimum. The algorithm iterates over subsequent complete paths flown by the wing, and exploits the values of $\bar{F}$ and $\Delta\bar{F}$ measured in the current and past paths. See Algorithm 1. A more detailed algorithm that can be used in practice, and

Algorithm 1: Optimization/Adaptation

while *true* **do**
    if *one complete loop flown* **then**
        calculate $\Delta\bar{F}$ and $\bar{F}$
        if $|\Delta\bar{F}| > \Delta\bar{F}_{min}$ **then**
            $\min_{\varphi_c} \quad |\Delta\bar{F}|$
            update φ_c
        else
            $\max_{\vartheta_c} \quad \bar{F}$
            update ϑ_c
        end
    end
end

has been tested in experiments, is given in the Appendix. The algorithm uses a coordinate search approach, see e.g. [26], to solve the two subsequent optimization problems, since no gradient information is available. The algorithm first checks if the absolute value of the traction force difference, $\Delta\bar{F}$, is smaller than some margin, $\Delta\bar{F}_{min}$. The latter is used as a stopping criterion for the φ direction adaptation. If this condition is not met, the algorithm adapts the value of φ_c in order to reduce the absolute value of the force difference, $|\Delta\bar{F}|$. Otherwise, the algorithm searches for the best vertical position ϑ_c, without changing φ_c. Apart from the convergence tolerances (see the Appendix for details), the scalar $\Delta\bar{F}_{min}$ is the only tuning parameter in our real-time optimization approach. If $\Delta\bar{F}_{min}$ is very small, the algorithm will tend to spend most of the time correcting the azimuthal position of the loop and the ϑ_c position would improve slowly. Vice versa, if $\Delta\bar{F}_{min}$ is large, most time is spent in correcting the average elevation position of the flown path.

V. Effects of Measurement Errors and Turbulence

The algorithm introduced in the previous section exploits the measurements of the tether force and wing position, and its performance will clearly depend on the accuracy of the related sensors, as well as on the intensity of wind turbulence. It is therefore of interest to study the effects of such phenomena.

First, we start with the description of the expected sensor errors, followed by an analysis of how much these errors affect the adaptation algorithm. Secondly, we will present the effects of added turbulence on the wind profile, and introduce measures to counteract its effects. We carry out these analyzes mainly with the simplified traction force model used in section III-A. We will also rely on simulation results employing the point-mass model of the wing to highlight specific effects, using a standard turbulence model which is common in wind turbine analysis.

A. Sensor Errors

For this analysis we assume that line angle sensors, measuring the orientation of the tethers with respect to the ground unit, are used to estimate the position of the wing. Moreover, an on-board inertial measurement unit can additionally be used to improve position data [27]. The line angle sensors are assumed to be optical encoders measuring the angle between the tethers and the ground, for the elevation angle ϑ, and between the projection of the tethers on the ground and the symmetry axis of the ground unit, for the azimuthal angle φ. Such encoders have various sources of errors and in general the accuracy is usually around ± 1 count, e.g an encoder with a 10 bit resolution has an additive error of less than $0.4°$. Assuming that the error at each time step is i.i.d. with zero mean, we can expect that the error on the center location of the path in φ and ϑ converges to zero for high sampling rates. Thus the calculation of the average traction force and average traction force difference is not influenced by the line angle measurements.

We next consider errors affecting the force measurements. Since the tether force is the main feedback variable used by our algorithm, we expect the related errors to be more critical for the performance of our adaptation approach. The force sensors are load cells installed at ground level, see e.g. [28] for details. The related measurement error is assumed to consist of two components, an additive term and a multiplicative term:

$$\tilde{F}(k) = F(k)(1+\delta_F) + \varepsilon_F(k)$$

δ_F accounts for a calibration error of the signal gain of the sensor and ε_F is an additive bias accounting for noise whose mean is a calibration offset. It is assumed that $|\delta_F| < 1$. Thus, for a sufficiently small sampling time the effects of the additive term ε_F on the average force become constant, such that this error term has no influence on the shapes of the average traction force and average traction force difference. Similarly, the multiplicative term δ_F does not influence the qualitative behavior of the average forces. While this is quite obvious for the total force, we show next that also the shape of the force difference is not affected.

The difference in average traction force can be written as

$$\Delta\tilde{\bar{F}} = \tilde{\bar{F}}_L - \tilde{\bar{F}}_R \tag{17}$$

where

$$\begin{aligned}\tilde{\bar{F}}_L &= \frac{1}{N_L}\sum_{k=1}^{N}\{\mathcal{C}v(\vartheta(k))m(\varphi(k)-\varphi_W)(1+\delta_F)+\varepsilon_F(k)|\varphi(k)\geq\varphi_c\} \\ \tilde{\bar{F}}_R &= \frac{1}{N_R}\sum_{k=1}^{N}\{\mathcal{C}v(\vartheta(k))m(\varphi(k)-\varphi_W)(1+\delta_F)+\varepsilon_F(k)|\varphi(k)<\varphi_c\}\,.\end{aligned} \tag{18}$$

Equations (17)-(18) can be simplified to

$$\Delta\tilde{\bar{F}}(\Theta,\varphi_W) = \tilde{\bar{F}}_L - \tilde{\bar{F}}_R \simeq -\frac{\mathcal{C}}{2}\sin(2(\varphi_c-\varphi_W))\tilde{\mathcal{B}}, \tag{19}$$

where the term $\tilde{\mathcal{B}}$ is given by

$$\begin{aligned}\tilde{\mathcal{B}} = &\frac{1}{N_L}\sum_{k=1}^{N}\{v(\vartheta(k))\sin(2|\varphi_\Delta(k)|)(1+\delta_F)|\varphi(k)\geq\varphi_c\} \\ &+\frac{1}{N_R}\sum_{k=1}^{N}\{v(\vartheta(k))\sin(2|\varphi_\Delta(k)|)(1+\delta_F)|\varphi(k)<\varphi_c\}\end{aligned}$$

From (19) we see that the qualitative behavior of $\Delta\tilde{\bar{F}}$ as a function of φ is the same as that of the true values, hence the alignment in φ direction is not affected by the force sensor errors, see Fig. 15 for a simulation example.

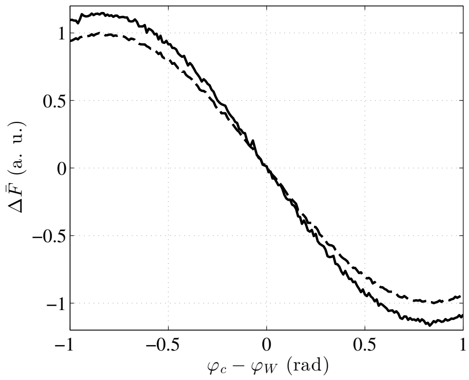

Fig. 15. Simulation results. Difference in average traction force $\Delta\bar{F}$ as a function of the misalignment between the average loop location and the wind direction, computed using the point-mass model with $\delta_F = 0.15$, $\varepsilon_F = 250 \pm 100$ N (normally distributed). The true $\Delta\bar{F}$ (dashed) and measured $\Delta\tilde{\bar{F}}$ (solid) are shown.

For the alignment in ϑ direction, we consider the difference of the average traction force of two loops at different elevation angle ϑ_c, since such a difference is used in our approach to compute the search direction for ϑ_c. Also in this case, it can be shown that the considered force sensor errors do not affect the alignment algorithm. In fact, the additive error term cancels out again and the multiplicative error only changes the magnitude of the difference of the average forces measured in the two flown loops, but not the sign (which is used in the optimization/adaptation algorithm), i.e. the qualitative behavior of the measured force as a function of ϑ_c is the same as that of the true force, see Fig. 16 for an example.

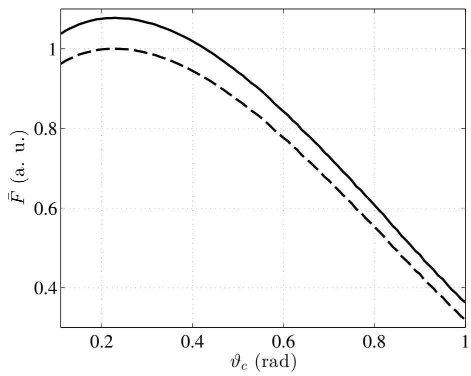

Fig. 16. Simulation results. Average traction force $\bar{F}$ as a function of the average loop elevation ϑ_c, computed using the point-mass model with $\delta_F = 0.15$, $\varepsilon_F = 250 \pm 100$ N (normally distributed). The true $\bar{F}$ (dashed) and the measured $\tilde{\bar{F}}$ (solid) are shown.

B. Turbulences

In a real-world system, the incoming wind will never be perfectly smooth and some fluctuations, such as wind gusts or turbulences, will be present. Using the wind shear profile (1), this can be expressed as

$$W_t(k,\varphi,\vartheta) = W_0\left(\frac{r\sin(\vartheta)}{Z_0}\right)^{\alpha} + W_\Delta(k,\varphi,\vartheta)$$

where W_t stands for the wind profile with added turbulences and W_Δ is the change in wind speed around the nominal wind value due to turbulences for a given point in time and space. For the sake of simplicity of notation, we omitted the sampling time k for the position angles φ and ϑ. As it can be seen from (6), changes in the wind speed influence the traction force quadratically. Thus, W_Δ will significantly affect the traction force developed by the wing and, consequently, the performance that can be achieved by the adaptation algorithm.

Turbulences are a very complex phenomena, for which a theoretical analysis is difficult to carry out. On the other hand, there exist state-of-the-art turbulence models readily available in public toolboxes, such as TurbSim [29]. These can be used to study the effects of turbulences on the system and on the adaptation algorithm via simulations. The wind fields generated with TurbSim, which is a tool used for wind mill analysis, use a measure for the turbulence strength called intensity I, defined as

$$I = \frac{u'}{U},$$

where U is the mean velocity and u' is the root-mean-square of the turbulent velocity fluctuations. A turbulence intensity of 10% and more is generally considered as strong and 1% to 5% as medium. The generated wind fields provide us with a value of W_Δ at each sampling time and any point in space. We used TurbSim with the Kaimal power spectrum to generate the turbulence values W_Δ, see Fig. 17 (details about the turbulence model can be found in [29]).

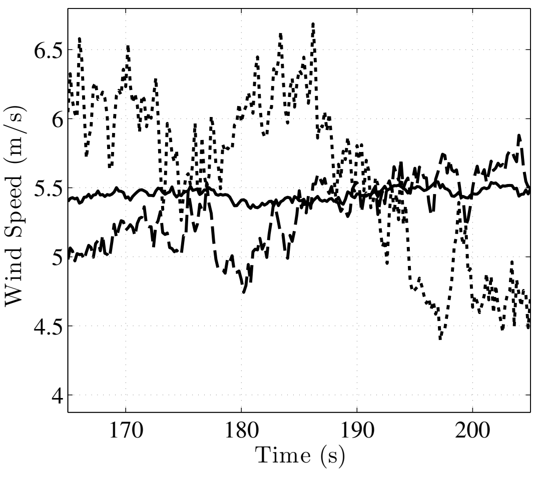

Fig. 17. Simulated turbulent wind speed in longitudinal direction over time for three different turbulence intensities with a average wind speed of 5.4 m/s, 1% (solid), 5% (dashed), and 10% (dotted).

Due to the turbulent wind, the traction forces experienced during flight will unlikely be equal to their nominal values $\bar{F}$ and $\Delta\bar{F}$, rather they will lie in an interval around such nominal values, see Figs. 18 and 19.

Regarding the φ_c alignment, i.e. seeking the optimal azimuthal position of the flown path, the presence of turbulence gives rise to a range, $\Delta\varphi_c$, of φ_c values for which a measure of $\Delta\bar{F} = 0$ is possible:

$$\Delta\varphi_c = \max(\varphi_c|\Delta\bar{F} = 0) - \min(\varphi_c|\Delta\bar{F} = 0),$$

Thus $\Delta\bar{F} = 0$ does not imply that the average loop location is aligned with the nominal wind, i.e. $\varphi_c = \varphi_W$. Within these azimuthal average positions, the optimization algorithm might make a step in the wrong direction, see Fig. 18. Estimating $\Delta\varphi_c$ is not straightforward, since it depends on the current wind situation at the wing's position. However, we can reduce the size of $\Delta\varphi_c$ at the expense of convergence speed. In particular, an intuitive idea to increase the robustness of the approach against turbulences is to use averaged quantities over more than a single flown loop. This means, instead of comparing the values of a single loop, $N_{avg} > 1$ loops are measured before the average values of $\Delta\bar{F}$ and $\bar{F}$ are calculated. With this approach, equations (12) and (14) become:

$$\bar{F}(\Theta,\varphi_W) = \frac{1}{N_{avg}N}\sum_{j=1}^{N_{avg}}\sum_{k=1}^{N} F_j(k)$$

$$\Delta\bar{F}(\Theta,\varphi_W) = \frac{1}{N_{avg}}\sum_{j=1}^{N_{avg}} \bar{F}_{L,j} - \bar{F}_{R,j},$$

where $F_j(k)$ stands for the instantaneous traction force during loop j at time k, and $\bar{F}_{L,j}$ and $\bar{F}_{R,j}$ are the averaged force values of the left and right half loop measured during the j-th completed loop, similar as in (13).

This modification can easily be integrated into Algorithm 1, by changing the first *if* statement on line 2, which then exploits the data from N_{avg} loops, instead of just one, to calculate the average force values.

In Fig. 18, the values of $\Delta\bar{F}$ as a function of φ_c in a turbulent wind flow are shown, for the case $N_{avg} = 1$ (gray dots). The same figure shows the envelope of $\Delta\bar{F}$ obtained with $N_{avg} = 5$. It can be noted that in this case the use of $N_{avg} = 5$ decreases $\Delta\varphi_c$ by almost a factor of two.

An example of the effect that N_{avg} has on $\Delta\varphi_c$ for different turbulence intensities is shown in Fig. 20. For this analysis, 100 different turbulent wind fields were generated. The point-mass model controlled by controller K was then simulated for 300 s. The collected data was used to estimate the range $\Delta\varphi_c$. It can be seen that $N_{avg} = 5$ gives already a good improvement for strong turbulences.

Finally, the presence of turbulence gives place to an envelope of uncertain values also for the total traction force. Also in this case, the use of more loops for the averaging leads to a reduction of such uncertainty, as shown in Fig. 19.

C. Discussion

We showed that errors in the line angle and force sensors do not impair the performance of our adaptation algorithm. For the line angle sensor errors, we only considered an additive error with zero mean. Systematic constant errors, such as misalignment of the sensors, do not affect the performance of the algorithm since they would introduce an offset in the

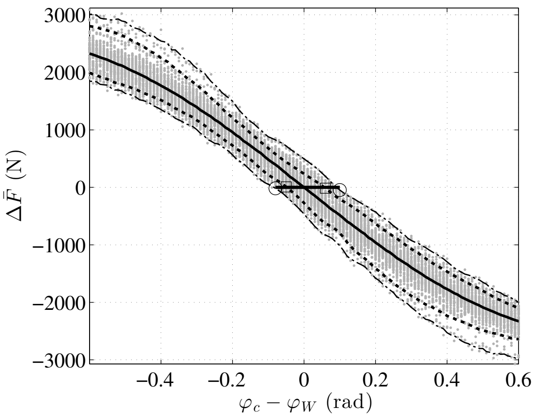

Fig. 18. Simulation results. Average traction force differences using the point-mass model for different values of φ_c, with $\vartheta_c = \arctan(\sqrt{\alpha})$, $W_0 = 5\,\text{m/s}$, $I = 5\%$. $\Delta\bar{F}$ with no turbulences (solid), $\Delta\bar{F}$ for turbulent wind flow (gray dots), the envelope of $\Delta\bar{F}$ obtained by using $N_{avg} = 1$ (dash-dot) and $N_{avg} = 5$ (dotted), and $\Delta\varphi_c$ (horizontal line) for $N_{avg} = 1$ (between circles) and for $N_{avg} = 5$ (between squares).

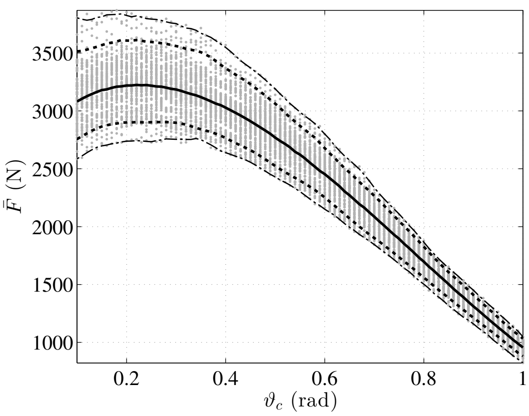

Fig. 19. Simulation results. Average traction forces using the point-mass model for different values of ϑ_c, with $\varphi_c = \varphi_W$, $W_0 = 5\,\text{m/s}$, $I = 5\%$. $\bar{F}$ with no turbulences (solid), $\bar{F}$ for turbulent wind flow (gray dots), the envelope of $\bar{F}$ obtained by using $N_{avg} = 1$ (dash-dot) and $N_{avg} = 5$ (dotted).

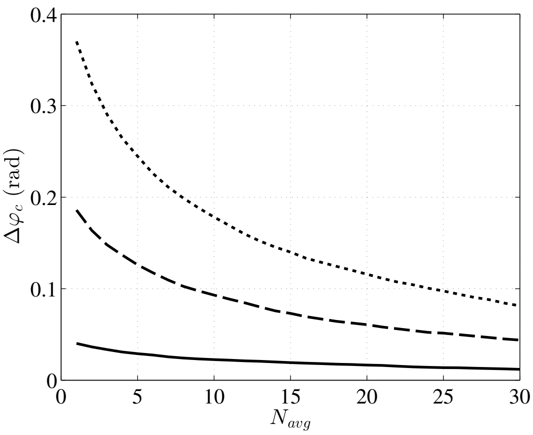

Fig. 20. Simulations results. Value of $\Delta\varphi_c$ with different turbulence intensities for different values of N_{avg} obtained using the point-mass model. Three different turbulence intensities are shown: 1% (solid), 5% (dashed), 10% (dotted).

TABLE I
POINT-MASS MODEL PARAMETERS USED FOR THE NUMERICAL SIMULATIONS

A	=	9 m	m	=	2.45 kg	r	=	30 m
n_l	=	3	d_l	=	0.003 m			
C_L	=	0.8	C_D	=	0.134	$C_{D,l}$	=	1.2
W_0	=	5 m/s	Z_0	=	4 m	α	=	0.1

force-position curves without altering their qualitative shape, which is exploited by our approach.

For the force sensor errors, we considered a constant multiplicative error and an additive error. Again, these errors do not affect the adaptation algorithm, since the qualitative system behavior is unaffected. Note that we assumed in both cases a fast sampling rate such that errors from high frequency noise get averaged out over the course of one flown (half-) path. To this end, in our experience a sampling rate of 50 Hz is sufficiently large to make errors on the computation of the average traction forces negligible.

As a last point, we analyzed the effect of turbulent wind on the adaptation algorithm using a dynamical point-mass model in simulation where the turbulent wind was generated with TurbSim. We showed that turbulences can cause the algorithm to make steps in the wrong direction around the optimal average location. The range of positions where this can happen increases with the turbulence intensity I, but it can be reduced in size by using averaged traction forces over multiple flown loops. Additionally, the stopping criterion $\Delta\bar{F}_{min}$ for the azimuthal position adaptation (see Algorithm 1) can be used as a tuning parameter to reduce steps in the wrong direction.

VI. NUMERICAL SIMULATIONS AND EXPERIMENTAL RESULTS

We tested the adaptation approach in simulation using the same point-mass dynamical model of the system as in [13] and the controller presented in [23]. The results indicate that the approach is able to tune in real-time the underlying controller K in order to follow a changing wind direction and adapt the paths' average elevation according to the (unknown) wind profile. The main parameters of the model are listed in Table I.

According to the simulations, the approach performs well in a turbulent wind field with an appropriate choice of N_{avg}. A plot with the time course of the average location of the path and the wind direction in such conditions with $N_{avg} = 3$ and $N_{avg} = 5$ can be seen in Fig. 21.

Additionally, simulation results show that wider loops perform better in turbulent wind situations. This is due to the fact that each half-loop takes longer to complete and thus turbulences get averaged out more than on shorter paths in time. This goes along the same direction as increasing N_{avg}.

The choice of N_{avg} and the loop period T influence the rate of convergence of the algorithm for changing wind situations.

Experimental test flights using the presented algorithm have also been carried out on a small scale prototype (shown in Fig. 22), built at UC Santa Barbara, with promising results. The prototype used two different three-line, inflatable kites with a constant tether length of $r = 30\,\text{m}$. The employed power kites were Airush One $6\,\text{m}^2$ and $9\,\text{m}^2$ kites. Due to the short

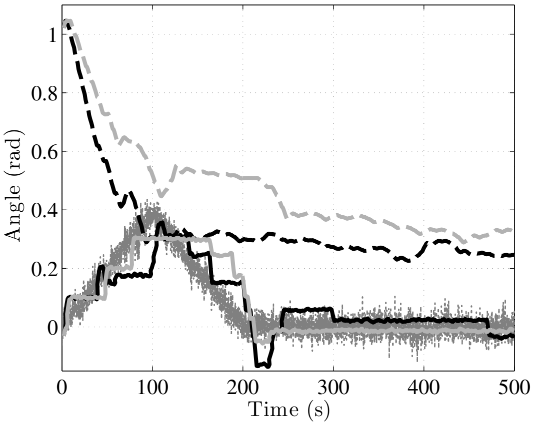

Fig. 21. Simulation results obtained by applying the proposed algorithm on the point-mass model with turbulent wind with intensity 5% with $N_{avg} = 3$ (black) and $N_{avg} = 5$ (light gray). The solid and dashed lines represent the average φ and ϑ positions of the path, φ_c and ϑ_c, respectively. The gray dotted line shows the true, turbulent wind direction.

Fig. 22. Small-scale prototype built at the University of California, Santa Barbara, to study the control of tethered wings for airborne wind energy.

lines, a measurement of φ_W with good accuracy, to be used to evaluate the performance of the adaptation approach, was possible with an anemometer installed at 4 m above the ground. The algorithm was set to use $N_{avg} = 3$. For more details on the test setup, see [23] and [28].

A test flight with the 9 m^2 kite is reported in Figs. 23-26. The underlying controller was initialized to fly a path with a misalignment of roughly 20° from the wind direction φ_W and with a overly high elevation. The algorithm was able to correct the misalignment with the wind direction in the first 150 s, i.e. roughly 30 flown loops, and then to adapt the azimuthal position according to wind direction changes while improving the average elevation, see Fig. 23. The initial and final paths of the wing with the measured trajectory (φ_c, ϑ_c) can be seen in Fig. 24. Note that although the paths seem not to differ much in position, yet the force increase is significant, see Fig. 25, as expected from the sensitivity analysis presented in section III. The corresponding wind speed during the test flight can be seen in Fig. 26, with an average value of 5.3 m/s. Note that due to the alignment with the wind the loop becomes more symmetric, thus indicating that measures of elapsed time or speed of the wing in a half path could also potentially be used, instead or in addition to the force, to detect a misalignment with the wind direction.

A test flight with the 6 m^2 kite, which was initially commanded to fly a path with a misalignment of roughly 25° from the wind direction φ_W and with a overly high elevation, is reported in Figs. 27-30. Also in this case, the algorithm was able to first correct the misalignment with the wind and then to improve the traction force by changing ϑ_c. A short movie of the test with the adaptive algorithm and this kite is also available online [30]. In Fig. 27, the time courses of the wind direction φ_W and of the average position φ_c and ϑ_c of the path, modified in real-time by the proposed algorithm, can be seen. In Fig. 28, the corresponding average traction force for each full path is shown. It can be noted that the average force increases significantly thanks to the adaptive approach. The time course of the wind speed magnitude is shown in Fig. 29. Finally, Fig. 30 shows two measured flown paths, at the beginning and at the end of the test flight, together with the optimal location in terms of average angle φ_c and with the measured trajectory of (φ_c, ϑ_c).

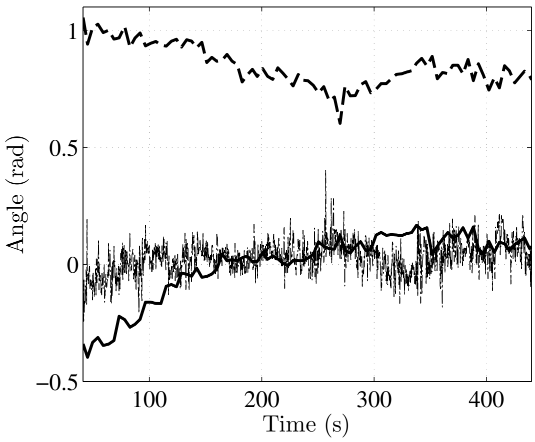

Fig. 23. Experimental test results using a small-scale prototype with a 9 m^2 kite. The φ_c position (solid) and ϑ_c position (dashed) of the paths, and the wind direction φ_W (dotted) are shown.

VII. Conclusions

We presented a study of the average traction force generated by a tethered wing and, based on the results of such analysis, we proposed an algorithm to adapt and optimize in real-time the average position of the flown path without exact knowledge of the wind direction and profile. The algorithm is not dependent on the system configuration, e.g. number of lines or position of the generator, and it can be used as an extension of any working controller for a tethered wing, provided that

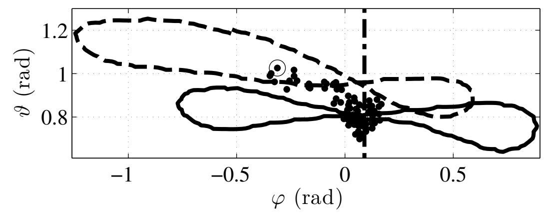

Fig. 24. Experimental test results using a small-scale prototype with a 9 m^2 kite. Initial (dashed) and final (solid) paths flown by the wing corresponding to the data shown in Figs. 23, 25, and 26. The trajectory of (φ_c, ϑ_c) (dotted) and the initial and final (φ_c, ϑ_c) locations (circles) are shown together with the optimal φ_c^* location (dashed-dotted).

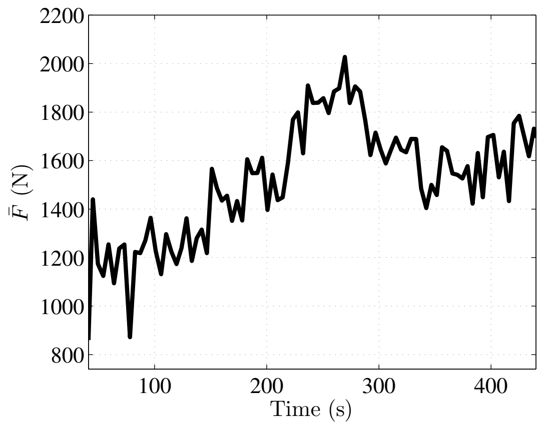

Fig. 25. Experimental test results using a small-scale prototype with a 9 m^2 kite. Course of the average traction force $\bar{F}$.

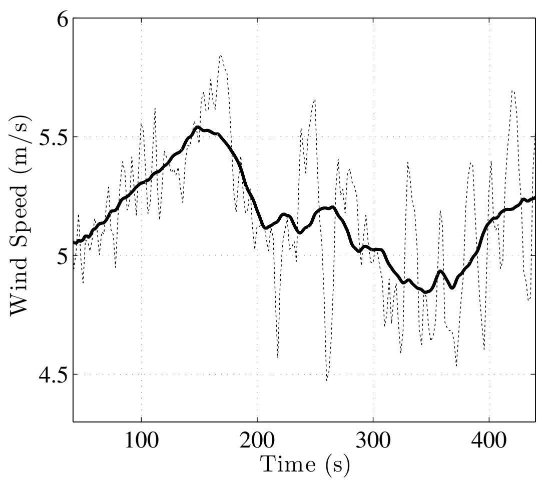

Fig. 26. Experimental test results using a small-scale prototype with a 9 m^2 kite. Course of wind speed measured roughly 4 m above the ground (dotted) and a moving average over 1 min (solid). The average wind speed was 5.3 m/s.

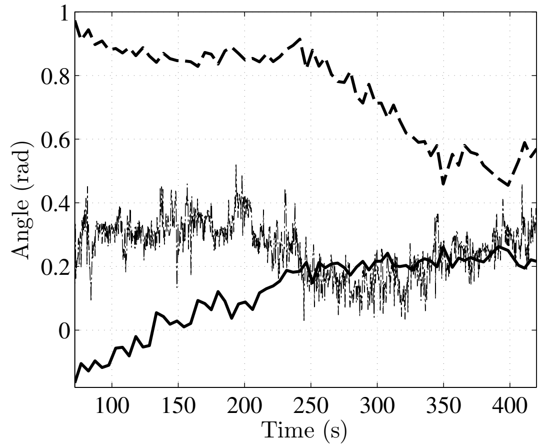

Fig. 27. Experimental test results using a small-scale prototype with a 6 m^2 kite. The φ_c position (solid) and ϑ_c position (dashed) of the paths, and the wind direction φ_W (dotted) are shown.

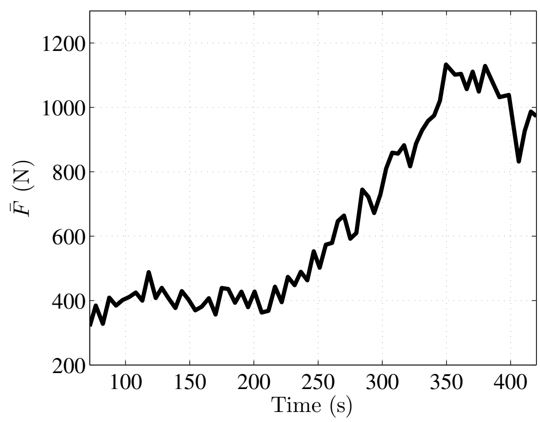

Fig. 28. Experimental test results using a small-scale prototype with a 6 m^2 kite. Course of the average traction force $\bar{F}$.

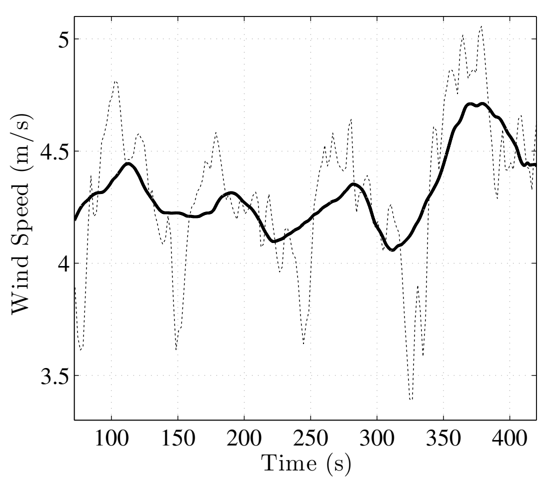

Fig. 29. Experimental test results using a small-scale prototype with a 6 m^2 kite. Course of wind speed measured roughly 4 m above the ground (dotted) and a moving average over 1 min (solid). The average wind speed was 4.3 m/s.

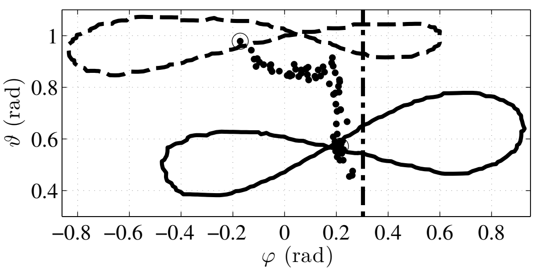

Fig. 30. Experimental test results using a small-scale prototype with a $6\,\mathrm{m}^2$ kite. Initial (dashed) and final (solid) paths flown by the wing corresponding to the data shown in Figs. 27-29. The trajectory of (φ_c, ϑ_c) (dotted) and the initial and final (φ_c, ϑ_c) locations (circles) are shown together with the optimal φ_c^* location (dashed-dotted).

the controller is able to control the wing in order to fly on a symmetric horizontal path and to attain a reference position in terms of average location of the path in the wind window. We tested the approach both with numerical simulations and real-world experiments, showing good performance in adapting and optimizing the system's operation in the presence of unknown and changing wind conditions with turbulences. The approach assumes that a constant line speed is used. If a different reeling strategy is adopted, like constant torque or speed-dependent torque, the approach presented here can still be used with minor modifications, in particular by using the generated power instead of the traction force as feedback variable.

Appendix
Detailed Adaptation Algorithm

The outline of the Algorithm 2 below is a more detailed version of Algorithm 1. Note that this algorithm uses N_{avg} loops to calculate the average forces. For path-related variables, we use i as the index standing for the last N_{avg} flown full paths, e.g. $\bar{F}(i)$ is the average traction force of the last N_{avg} paths and $\vartheta_c(i)$ the average ϑ position of the last N_{avg} paths. The employed coordinate search method uses the step sizes δ_φ and δ_ϑ for the adaptation of the φ_c and ϑ_c directions, respectively. Both step sizes have a defined minimal and maximal value, denoted by a subscript *min* or *max*. At each change in φ_c or ϑ_c, the related step size is adapted with a scaling factor $c > 1$ (if the step direction is unchanged) or $1/c$ (if the step direction changes). Finally, there exists a lower limit for the ϑ_c value, denoted as ϑ_c^{min}, to prevent the wing from flying too close to the ground.

Algorithm 2: Optimization/Adaptation - Detailed

while *true* **do**
  if N_{avg} *complete loops flown* **then**
    if $|\Delta\bar{F}(i)| > \Delta\bar{F}_{min}$ **then**
      if $\Delta\bar{F}(i) > 0$ **then**
        if $\Delta\bar{F}(i-1) > 0$ **then**
          $\delta_\varphi = \min\{\delta_{\varphi,max}, c\,\delta_\varphi\}$
        else
          $\delta_\varphi = \max\{\delta_{\varphi,min}, \frac{1}{c}\delta_\varphi\}$
        end
        $\varphi_c(i+1) = \varphi_c(i) + \delta_\varphi$
      else /* $\Delta\bar{F}(i) < 0$ */
        if $\Delta\bar{F}(i-1) < 0$ **then**
          $\delta_\varphi = \min\{\delta_{\varphi,max}, c\delta_\varphi\}$
        else
          $\delta_\varphi = \max\{\delta_{\varphi,min}, \frac{1}{c}\delta_\varphi\}$
        end
        $\varphi_c(i+1) = \varphi_c(i) - \delta_\varphi$
      end
    else /* $|\Delta\bar{F}(i)| \leq \Delta\bar{F}_{min}$ */
      if $\bar{F}(i-1) < \bar{F}(i)$ **then**
        $\delta_\vartheta = \min\{\delta_{\vartheta,max}, c\,\delta_\vartheta\}$
        if $\vartheta_c(i-1) > \vartheta_c(i)$ **then**
          $\vartheta_c(i+1) = \vartheta_c(i) - \delta_\vartheta$
        else
          $\vartheta_c(i+1) = \vartheta_c(i) + \delta_\vartheta$
        end
      else /* $\bar{F}(i-1) \geq \bar{F}(i)$ */
        $\delta_\vartheta = \max\{\delta_{\vartheta,min}, \frac{1}{c}\delta_\vartheta\}$
        if $\vartheta_c(i-1) > \vartheta_c(i)$ **then**
          $\vartheta_c(i+1) = \vartheta_c(i) + \delta_\vartheta$
        else
          $\vartheta_c(i+1) = \vartheta_c(i) - \delta_\vartheta$
        end
      end
      $\vartheta_c(i+1) = \max\{\vartheta_c^{min}, \vartheta_c(i+1)\}$
    end
  end
end

References

[1] M. Diehl, R. Schmehl, and U. Ahrens, Eds., *Airborne Wind Energy*, ser. Green Energy and Technology. Springer Berlin Heidelberg, 2014.

[2] L. Fagiano and M. Milanese, "Airborne wind energy: an overview," in *American Control Conference 2012*, Montreal, Canada, 2012, pp. 3132–3143.

[3] M. L. Loyd, "Crosswind kite power," *Journal of Energy*, vol. 4, no. 3, pp. 106–111, May 1980.

[4] Makani Power Inc., [Online], Alameda, CA, USA, Sep. 2013, available: http://www.makanipower.com/.

[5] Sky Sails GmbH & Co., [Online], Hamburg, Germany, Sep. 2013, available: http://www.skysails.info/.

[6] Ampyx Power, [Online], Den Haag, The Netherlands, Sep. 2013, available: http://www.ampyxpower.com/.

[7] Windlift, Inc., [Online], Raleigh, NC, USA, Sep. 2013, available: http://www.windlift.com/.

[8] Kitenergy S.r.l., [Online], Turin, Italy, Sep. 2013, available: http://www.kitenergy.net/.

[9] Enerkite GmbH, [Online], Berlin, Germany, Sep. 2013, available: http://www.enerkite.de/.

[10] Swiss Kite Power, [Online], Windisch, Switzerland, Sep. 2013, available: http://www.swisskitepower.ch/.

[11] M. Canale, L. Fagiano, and M. Milanese, "Power Kites for Wind Energy Generation," *IEEE Control Systems Magazine*, vol. 27, no. 6, pp. 25–38, Dec. 2007.

[12] A. Ilzhöfer, B. Houska, and M. Diehl, "Nonlinear MPC of kites under varying wind conditions for a new class of large-scale wind power generators," *Int J Robust Nonlinear Control*, vol. 17, pp. 1590–1599, Nov. 2007.

[13] M. Canale, L. Fagiano, and M. Milanese, "High altitude wind energy generation using controlled power kites," *IEEE Transactions on Control Systems Technology*, vol. 18, no. 2, pp. 279 –293, Mar. 2010.

[14] E. Terink, J. Breukels, R. Schmehl, and W. Ockels, "Flight dynamics and stability of a tethered inflatable kiteplane," *AIAA Journal of Aircraft*, vol. 48, no. 2, pp. 503–513, Mar. 2011.

[15] C. Vermillion, T. Grunnagle, and I. Kolmanovsky, "Modeling and control design for a prototype lighter-than-air wind energy system," in *American Control Conference (ACC)*, 2012, pp. 5813–5818.

[16] J. H. Baayen and W. J. Ockels, "Tracking control with adaption of kites," *IET Control Theory Appl*, vol. 6, no. 2, pp. 182–191, 2012.

[17] P. Williams, B. Lansdorp, and W. Ockels, "Optimal crosswind towing

and power generation with tethered kites," *Journal of Guidance Control and Dynamics*, vol. 31, no. 1, pp. 81–93, Jan. 2008.

[18] B. Houska and M. Diehl, "Optimal control for power generating kites," in *European Control Conference (ECC), Kos, Greece, 2.-5. July*, 2007.

[19] S. Costello, G. Franois, and D. Bonvin, "Real-time optimization for kites," in *Proceedings of the IFAC Workshop on Periodic Control Systems, Caen, France, 3.-5. July*, 2013, pp. 64–69.

[20] M. Diehl, "Real-time optimization for large scale processes," Ph.D. dissertation, Dept. Natural Science and Mathematics, Ruprecht-Karls-Universität Heidelberg, Heidelberg, Germany, June 2001.

[21] L. Fagiano, "Control of tethered airfoils of high-altitude wind energy generation," Ph.D. dissertation, Dept. Control Comput. Eng., Politecnico di Torino, Torino, Italy, 2009.

[22] M. L. Ray *et al.*, "Analysis of wind shear models and trends in different terrains," in *AWEA Proceedings of AWEA Windpower 2006 Conference, 4.-7. June*, Pittsburgh, PA, 2006.

[23] L. Fagiano, A. U. Zgraggen, M. Morari, and M. Khammash, "Automatic crosswind flight of tethered wings for airborne wind energy: Modeling, control design, and experimental results," *IEEE Transactions on Control Systems Technology*, vol. 22, no. 4, pp. 1433–1447, July 2014.

[24] L. Fagiano, M. Milanese, and D. Piga, "Optimization of airborne wind energy generators," *International Journal of Robust and Nonlinear Control*, vol. 22, no. 18, pp. 2055–2083, Dec. 2012.

[25] S. Boyd and L. Vandenberghe, *Convex Optimization*. Cambridge, U.K.: Cambridge University Press, 2004.

[26] A. R. Conn, K. Scheinberg, and L. N. Vicente, *Introduction to Derivative-Free Optimization*. Philadelphia, PA, USA: Society for Industrial and Applied Mathematics, Jan. 2009.

[27] L. Fagiano, K. Huynh, B. Bamieh, and M. Khammash, "On sensor fusion for airborne wind energy systems," *IEEE Transactions on Control Systems Technology*, vol. 22, no. 3, pp. 930–943, May. 2014.

[28] L. Fagiano and T. Marks, "Design of a Small-Scale Prototype for Research in Airborne Wind Energy," *IEEE/ASME Transactions on Mechatronics*, 2014, in press, available online at IEEEXplore.

[29] N. Kelley and B. Jonkman, NWTC Computer-Aided Engineering Tools - TurbSim, http://wind.nrel.gov/designcodes/preprocessors/turbsim/, accessed 12-July-2013.

[30] EISG project "Autonomous flexible wings for high-altitude wind energy generation", experimental test movie, October 2012. Available on–line: http://youtu.be/5prsTSiLFIw.

Aldo Zgraggen received the B.S. and M.S. degree in mechanical engineering from ETH Zurich, Zurich, Switzerland, in 2007 and 2009, respectively.

He was with the Control and Dynamical Systems Group, California Institute of Technology, Pasadena, CA, USA, from 2008 to 2009. Since 2009, he has been a Ph.D. student with the Automatic Control Laboratory of ETH Zurich. His current research interests include control of tethered wings for airborne wind energy generation.

Lorenzo Fagiano (M'07) received the MS degree in Automotive Engineering in 2004 and the Ph.D. in Information and Systems Engineering in 2009 from Politecnico di Torino, Italy. In 2005 he worked for Fiat Research Centre, Italy, in the field of active vehicle systems. In 2007 he was a visiting scholar at the Katholieke Universiteit Leuven. From 2009 to 2010 he was a post-doctoral researcher at Politecnico di Torino. From 2010 to 2012 he was a visiting researcher at the University of California, Santa Barbara, and from 2012 to 2013 a senior researcher at the Automatic Control Laboratory, ETH Zurich. Lorenzo Fagiano is currently a scientist at ABB Switzerland, Corporate Research. His research interests include switchgear systems, airborne wind energy, model predictive control, experimental modeling. Lorenzo Fagiano is recipient of the 2011 IEEE Transactions on Systems Technology Outstanding Paper Award, of the 2010 ENI award "Debut in Research" prize, of the Maffezzoni prize 2009 and of a Marie Curie International Outgoing Fellowship.

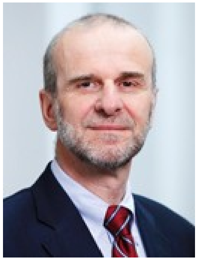

Manfred Morari (F'05) was head of the Department of Information Technology and Electrical Engineering at ETH Zurich from 2009 to 2012. He was head of the Automatic Control Laboratory from 1994 to 2008. Before that he was the McCollum-Corcoran Professor of Chemical Engineering and Executive Officer for Control and Dynamical Systems at the California Institute of Technology. He obtained the diploma from ETH Zurich and the Ph.D. from the University of Minnesota, both in chemical engineering. His interests are in hybrid systems and the control of biomedical systems. In recognition of his research contributions he received numerous awards, among them the Donald P. Eckman Award, the John R. Ragazzini Award and the Richard E. Bellman Control Heritage Award of the American Automatic Control Council, the Allan P. Colburn Award and the Professional Progress Award of the AIChE, the Curtis W. McGraw Research Award of the ASEE, Doctor Honoris Causa from Babes-Bolyai University, Fellow of IEEE, IFAC and AIChE, the IEEE Control Systems Technical Field Award, and was elected to the National Academy of Engineering (U.S.). Manfred Morari has held appointments with Exxon and ICI plc and serves on the technical advisory boards of several major corporations.